Melt–clast interaction and power-law size distribution of clasts in pseudotachylytes

Sumit Kumar Ray*

Geological Survey of India, Central Headquarters, 27 J L Nehru Road, Kolkata 700 016, India

Abstract

Before the onset of melting along frictional interfaces, the wall rocks of seismic faults are crushed to generate a power-law grain-size distribution pattern. Theoretical analysis with the help of numerical models shows that, under conditions of uniform rim melting of the grains, the pre-melting power-law pattern survives in a modified form in the relicts, which occur as clasts in the quenched product, i.e. pseudotachylyte. The size distribution of clasts in experimentally produced as well as natural pseudotachylytes, including those from the Sarwar–Junia fault zone in western India, shows a pattern similar to that predicted by theoretical analysis. A micron-scale mantle of glass ± microlites around a large number of clasts, and minute beads of glass set within glassy matrix, are the observed evidence of rim melting. Post-melting clast size distribution in the numerical models follows the relationship $N \propto (1 + z/z')^{-D}$, where N is number of clasts of size $\geq z$. Size z may be represented by mean diameter r, or sectional area a, or volume v, and $D(= D^r, D^a$ or $D^v)$ is the modified power-law exponent. $z' (= r', a'$ or $v')$ is a constant that depends on thickness (ω) of uniform rim melting, and $r' = \omega$, $a' = \omega^2$, and $v' = \omega^3$. The analysis suggests that the modified power-law clast-size distribution pattern is a characteristic feature of all fault-related pseudotachylytes.
© 2004 Elsevier Ltd. All rights reserved.

Keywords: Pseudotachylyte; Friction melting; Clast size; Power-law; India

1. Introduction

Brittle faulting may transform the fault wall rocks to comminuted rocks with or without pseudotachylyte, depending on whether frictional melt is generated along the slip interface or not. The common occurrences of pseudotachylytes as discordant veins in close association with fault zones, and the presence of igneous microtextures in the matrix (Shand, 1916; Philpotts, 1964; Maddock, 1983, 1986), are generally cited by geologists as evidence of rock melting by frictional heat generated along slip planes. Pseudotachylytes are interpreted as the quenched products of the melt, which may flow into adjacent rock openings and get emplaced as *injection veins*, or cool down at the sites of melt generation as *fault veins* (Sibson, 1975). Frictional heat generated along fault planes during earthquakes is adequate to melt wall rocks (McKenzie and Brune, 1972; Sibson, 1975; Spray, 1987, 1995), and so pseudotachylytes are widely accepted as indicators of palaeoseismic events.

Pseudotachylytes contain lithic clasts (Magloughlin and Spray, 1992) of varying sizes and proportions in a typically dark matrix. Shimamoto and Nagahama (1992) reported that the clasts obey a power-law size distribution pattern (i.e. $N \propto d^{-D}$, where N is the number of clasts with mean diameter $\geq d$, and D is the power-law exponent). Ray (1999), however, found that the distribution pattern in pseudotachylyte samples from the Sarwar–Junia sector in the Precambrian terrain of western India (Fig. 1), shows a slight departure from the power-law pattern, and so can be described as a modified power-law distribution. Instead of a straight-line graph, which is characteristic of power-law distributions, the log–log plots of size vs. cumulative frequency of the clasts yield a pattern of gently curved graphs because of a decrease in slope of the line (i.e. D value) towards the finer sizes. The modified pattern, according to some workers (Tsutsumi, 1999) can be expressed by the empirically determined equation $N = N'(1 + d/d')^{-D}$, where N' and d' are constants, and D is a power-law exponent. Ray (1999) concluded that this pattern is characteristic of only those pseudotachylytes that are formed by transformation of cataclastically deformed

* Tel.: +91-33-224-96993; fax: +91-33-224-96956.
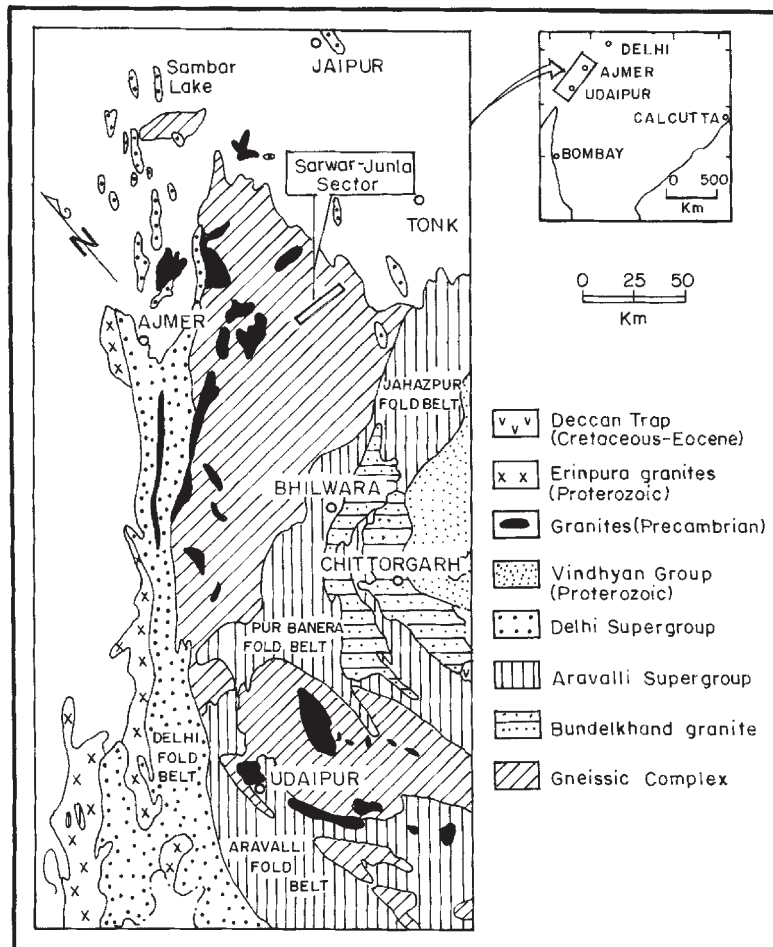 *E-mail address:* sumitkumarray@hotmail.com (S.K. Ray).

Fig. 1. Geological setting of the Sarwar–Junia sector in the Precambrian terrain of central Rajasthan, India (adapted from Balasundaram, 1969).

rocks by the pervasion of frictional melt. He inferred that the clasts and the finely crushed material in the matrix are products of grain-size reduction by cataclasis, which generates a fractal set of fragments that obeys power-law size distribution. A significant part of the matrix now consists of the quenched product of the melt that was generated by melting at slip interfaces. The melt pervaded the intergranular space of the crushed rocks, which by this process, were transformed to clast-laden pseudotachylytes. The transformed product inherited the power-law pattern of the comminuted parent rocks, with minor modifications. Rim melting of the clasts because of heat transfer from the pervading melt, modified the pattern. But the question remains as to whether a modified power-law clast-size distribution pattern is a characteristic feature of the particular variety, or all varieties of pseudotachylytes? Can the available genetic models of pseudotachylyte emplacement, in which the clasts are interpreted as relicts that survived melting, or occasional wall rock fragments entrained in the flowing melt, also explain this pattern? To what extent does post-cataclasis melting, which these models suggest, modify the pattern generated by early cataclasis? Or does melting completely destroy the pattern?

The theoretical analysis presented in this paper addresses these questions, and indicates that melting only modifies and does not destroy the power-law pattern, which may be a recognisable feature of the clast population of all varieties of fault-related pseudotachylytes, irrespective of the generation process involved.

The present paper also contains discussion on microstructures observed by scanning electron microscopy (SEM) and microprobe analysis of representative samples of the pseudotachylytes exposed in the Sarwar–Junia fault zone (Fig. 1). The microstructures helped in validation of the assumption of uniform rim melting applied in the theoretical models.

2. Geological setting

Pseudotachylytes and cataclasites exposed in a 20-km-long, 3–4-km-wide zone in the Sarwar–Junia sector of the Precambrian terrain of western India mark the Sarwar–Junia fault zone (Fig. 1). The general geological setting of the fault zone has been described in an earlier contribution (Ray, 1999). By applying image processing software

combined with GIS capabilities, Ray (1999) carried out microscopic scale clast size analysis of pseudotachylyte samples from the area. In the 2-D analysis, in which size was represented by area of the clasts in sections, it was observed that log–log plots of size vs. cumulative frequency yield broadly linear graphs, which flatten towards the finer clast sizes. It was concluded that the observed graph pattern reflects a modified power-law size distribution pattern, and is formed only in a particular genetic variety of pseudotachylytes (discussed above).

Rocks exposed in the area are heterogeneous biotite gneisses with sillimanite- and garnet-bearing schists and rare amphibolites belonging to the Banded Gneissic Complex (Heron, 1953; Geological Survey of India, 1977). These constitute the basement of the Precambrian gneissic terrain. The successively younger Proterozoic rocks of the Aravalli and Delhi Groups were deposited on the basement. Brittle faulting in the Sarwar–Junia sector has transformed gneissic wall rocks to cataclasites and pseudotachylytes. The pseudotachylyte veins are concordant as well as discordant to the gneissic foliation, and traverse intact country rock as well as the cataclasites. Pseudotachylyte veins show considerable variation in width and include veins of a few millimetres up to 10 cm wide. Networks of pseudotachylyte veins in proto-cataclasites are also common. The gneissic country rock affected by faulting has evolved through Precambrian polyphase deformation and metamorphism. Evidence of post-Precambrian regional metamorphism and deformation are absent. Absence of neomineralisation or recrystallisation in the glassy pseudotachylytes indicates that pseudotachylyte formation post-dates the Precambrian metamorphic episodes. Abundance of glass and microlites of high temperature minerals, like gedrites and hercynites (discussed later), indicates quenching, which in turn suggests a shallow depth of the faulting.

3. Theoretical analysis

With the onset of slip, the intact wall rocks of faults are crushed to generate rock fragments with a progressive reduction of fragment size. Sammis et al. (1987) applied a fragmentation model of particle-size reduction along fault interfaces, and generated simulated fault gouge, in which the particles have a fractal size distribution pattern. In artificial gouges produced by laboratory experiments, Marone and Scholz (1989) also recorded fractal distribution of the particles. By analogy, Ray (1999) concluded that grain-size reduction by cataclasis along fault interfaces is a self-similar process of progressive fragmentation, which generates particles with a power-law (= fractal) size–frequency distribution. This conclusion is in agreement with the general observation that fragmentation of objects by geological processes generates a fractal pattern (Turcotte, 1997). Because products of self-similar processes are scale

invariant (Turcotte, 1997), the distribution in any size fraction will show a power-law pattern.

3.1. Numerical model

Let us assume a crushed rock model in which the grain size, frequency (f) and cumulative frequency (cf) are distributed according to a power-law, as shown in Table 1a. For convenience of analysis let us consider that the grains are spherical. The radius r, and volume (V) and cumulative volume (cV) occupied by the grains of the different size fractions, are also given (Table 1a).

Log–log plots of size (v) vs. frequency (f), and size vs. cumulative frequency (cf) show straight-line graphs (Fig. 2a and b), whose general expression is:

$$\log N = c' - D\log v \tag{1}$$

where N represents number of grains (f) of size v (Fig. 2a), or grains (cf) of size $\geq v$ (Fig. 2b). D is slope of the straight line, and c' is a constant. This expression can be written as:

$$N = cv^{-D} \text{ or } N \propto v^{-D} \tag{2}$$

which is a general expression for a power-law distribution. Slope of the graph yields the power-law exponent D, which is 0.994 and 1.0 in Fig. 2a and b, respectively. Fig. 2a and b thus establishes that grains in the model obey a power-law size–frequency distribution pattern, and so simulate the distribution pattern in crushed rocks generated along fault interfaces.

3.2. The later stage: frictional melting

The favoured explanation for melting is that heat generated due to comminution at the frictional interfaces may accumulate because of low thermal conductivity of the rocks and so lead to melting Melting may affect the grains in such a way that both size and shape of each grain are modified, or only a rim of uniform thickness melts in each grain thereby reducing the size but retaining the shape. Rim melting may be possible if a grain is heated by uniform heat flow across the outer surface to the interior of the grain (Fig. 3). Because of uniform heat flow, the isotherms within the grain will be parallel to the grain boundary. If T_m is the melting temperature of the grain, a rim of thickness ω, which is defined by position of the isotherm T_m within the grain, will melt. Such a melting process will reduce size, but retain the shape of the grains. Grains with their longest dimension $\leq 2\omega$ will completely melt, whereas those with longest dimension $> 2\omega$ will have relics. Theoretically, ω should vary from grain to grain, depending on conductivity, specific heat, etc. As ω is small, variation of ω from grain to grain will be very small. However, melting of a rim of uniform thickness in all the grains has been assumed for determining statistics of size-distribution in the post-melting product.

Table 1
Effect of post-cataclasis melting on grain-size distribution pattern—numerical model. (a) Initial grain size distribution in the crushed-rock model. (b) Distribution after size reduction by melting (uniform reduction in r by 1 mm)

Grain size (volume in mm³) (v) (1)	Radius (in mm) (r) (2)	Frequency (f) (3)	Cumulative frequency (cf) (4)	Volume occupied by grains of the size fraction (in mm³) ($V = fv$) (5)	Cumulative volume occupied (in mm³) (cV) (6)	Cumulative volume of melt generated (in mm³) (7)
(a)						
1	0.6203	90000	100,000	90000	550,000	Nil
10	1.3364	9000	10000	90000	460,000	Nil
100	2.8793	900	1000	90000	370,000	Nil
1000	6.2032	90	100	90000	280,000	Nil
10000	13.3645	9	10	90000	190,000	Nil
100,000	28.7929	1	1	100,000	100,000	Nil
(b)						
–	(0.62–1.0)	–	–	– (90000)	–	309215.32
0.1596	0.3364	9000	10000	1436.4 (88563.6)	240784.68	219215.32
27.8057	1.8793	900	1000	25025.13 (64974.87)	239348.28	130651.72
590.1419	5.2032	90	100	53112.77 (36887.23)	214323.15	65676.85
7919.0775	12.3645	9	10	71271.70 (18728.3)	161210.38	28789.62
89938.68	27.7929	1	1	89938.68 (10061.32)	89938.68	10061.32

The figures in parenthesis in column 5 are the approximate volume of melt generated by uniform melting of a thin film of 1 mm thickness along the outer surface of each grain of the size fraction.
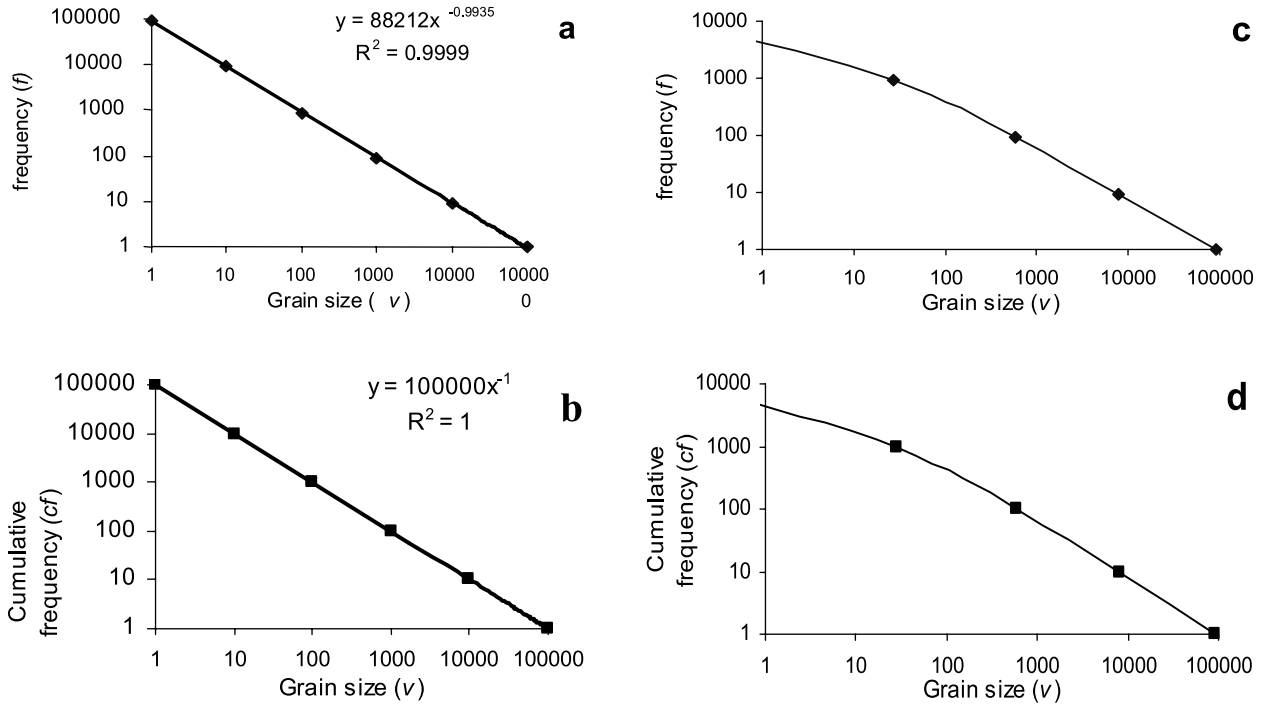
Fig. 2. Log–log graphs showing grain-size distribution pattern in the numerical model presented in Table 1a and b. (a) and (b) Distribution pattern in the parent crushed rock model (Table 1a); the solid lines are regression lines of the points of log–log plot of (a) size (v) vs. frequency (f), and (b) size vs. cumulative frequency (cf). Both are straight line graphs of R^2 value = 1 (see text) and give power-law exponents of 0.994 and 1.0, respectively. (c) and (d) Distribution pattern in the post-melting product of the numerical model (Table 1b); the line joins the points of the plots of (c) v vs. f and (d) v vs. cf in the post-meting product; all are gentle curves, indicating variable power-law exponent in each distribution. V, f and cf are as defined in Table 1.

3.2.1. The post-melting product: numerical model

Let us consider that melting affects the grain population (Table 1a) in such a way that a rim of uniform thickness of 1 mm melts in each grain. The post-melting size distribution will be as shown in Table 1b. All 90,000 grains with original $r = 0.6203$ mm will disappear because of their complete melting, generating melt of volume of approximately 90,000 mm³. The 9000 grains of original radius $r = 1.336$ mm will be reduced to relict grains with
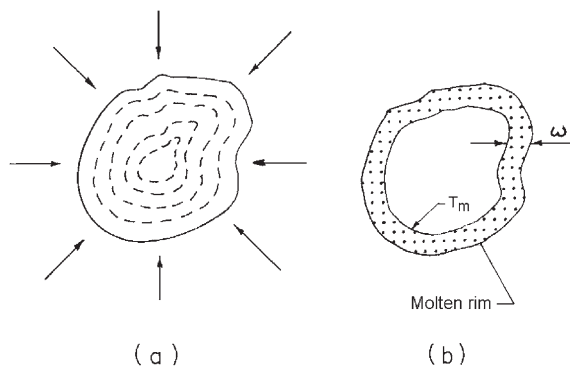

Fig. 3. Schematic diagram explaining rim melting of grains. (a) Temperature gradient towards the core will develop because of uniform heat flow across the outer surface to the interior of the grain. Isotherms within the grain will be parallel to the grain boundary (dashed lines). (b) Position of the isotherm T_m (melting temperature of the grain) determines thickness (ω) of the molten rim. Grains with diameter $\leq 2\omega$ will completely dissolve, whereas those with $> 2\omega$ will have relics.

$r = (1.336–1.0)$ mm and cover 1436.40 mm³ volume of the partly molten rock. Similarly the modified radius, volume, cumulative volume and approximate volume of melt generated by melting of the grains of each size fraction of the model have been calculated (Table 1b). Log–log graphs of size vs. frequency and size vs. cumulative frequency of the post-melting clast population are shown in Fig. 2c and d.

A comparison of the log–log graphs of pre-melting (Fig. 2a and b) and post-melting (Fig. 2c and d) size–frequency distributions in the numerical model reveals that the initial power-law distribution pattern is significantly modified, but still recognisable, in the surviving relics. In contrast to the straight-line graphs of initial frequency distributions (Fig. 2a and b), the post-melting graphs (Fig. 2c and d) are curvilinear. The straight-line graphs signify a uniform power-law exponent for the entire size range, whereas the curvilinear graphs indicate that melting destroys the scale invariant character and generates a distribution with variable power-law exponent. This variation again shows a non-linear pattern. A composite diagram (Fig. 4), showing the pre-melting and post-melting graphs, brings out details of the modification. The straight line AB represents the assumed initial grain-size distribution pattern taken from Fig. 2b, whereas the curve MNOP represents the pattern in the relict grains in Fig. 2d. The average slope of the segment M–N for size fraction M′–N′ is close to the slope of A–B. But it is lower in the size-fraction N′–O′ and further
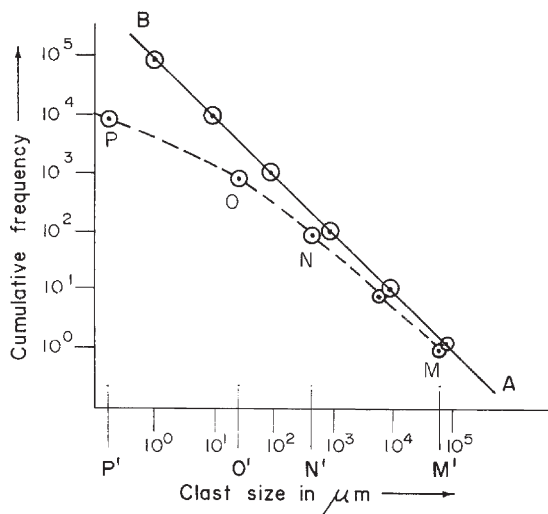
Fig. 4. A composite diagram showing pre-melting (AB) and post-melting (MNOP) graphs for comparison. AB and MNOP are taken from Fig. 2b and d, respectively. AB is straight line, signifying uniform power-law exponent. MNOP shows 'left-hand fall-off', signifying variable exponent, which increases from the finer to the coarser size fractions.

decreases in the still finer size fraction $O'-P'$. In other words the power-law exponent increases from the finer to the coarser size fractions (Table 2). The pattern may be described as 'left-hand fall-off' pattern of graphs obtained by log–log plot of size vs. cumulative frequency along the X and Y co-ordinate axes, respectively (Fig. 4). Gentle curvature of the graph indicates that for narrow clast-size ranges, a statistically valid power-law exponent can be determined.

3.2.2. The modified power-law exponent

Clast-size distribution in experimentally generated pseudotachylytes follows the relationship:

$$N = N'(1 + d/d')^{-D} \qquad (3)$$

where N is the number of clasts with diameter $\geqq d$, N' is a constant that depends on total number of measurements, and d' and D are material constants (Tsutsumi, 1999). Eq. (3) indicates that log–log plots of $(1 + d/d')$ vs. N will give a straight line graph, the slope of which will give a uniform D-value, which is the modified power-law exponent of the clast-size distribution. In most of the previous work on clast-size analysis, the size was measured and represented by mean diameter, or longest axis (Shimamoto and Nagahama, 1992; Tsutsumi, 1999), or area of clasts in thin sections (Ray, 1999). In the numerical models of the present study, the volume of clasts was also considered. The relationship between cumulative frequency (N) and clast size (z), where z is represented by radius (r), or sectional area (a), or volume (v) of the clasts in the post-melting clast population of the numerical model, is discussed in the following section.

The log N vs. log r, or vs. log v plots of the pre-melting size distribution of the clast sets in the models with all spherical clasts (Table 3) give straight line graphs (Fig. 5a

Table 2
Change of power-law exponent because of rim melting of grains of the numerical model

Grain size range in mm³	Size–frequency distribution		Size–cumulative frequency distribution	
	Power-law exponent in pre-melting distribution	Power-law exponent in post-melting product (pseudotachylyte)	Power-law exponent in pre-melting distribution	Power-law exponent in post-melting product (pseudotachylyte)
10–99	0.9935	0.446	1.0	0.446
100–999	0.9935	0.754	1.0	0.754
1000–9999	0.9935	0.887	1.0	0.881
10000–100,000	0.9935	0.904	1.0	0.948

Table 3

Numerical models showing the pattern of modification of initial power-law clast-size distributions by uniform rim melting, and properties of post-melting distribution

Model no.	Pre-melting distribution			Post-melting distribution							
	(Clast size) radius (r)	(Clast size) volume (v)	Cumulative frequency (N)	Thickness of uniform rim melting (ω)	(Clast size) radius (r)	R^2 value of regression line of U vs. N log–log plot[a]	(Clast size) sectional area (a)	R^2 value of regression line of A vs. N log–log plot[a]	(Clast size) volume (v)	R^2 value of regression line of V vs. N log–log plot[a]	Cumulative frequency (N)
IA	0.6203	1	100000	1.3 units	–	1.0	–	0.9935	–	0.9898	–
	1.3364	10	10000		0.0364		0.00416		0.0002		10000
	2.8793	100	1000		1.5793		7.8367		16.4996		1000
	6.2032	1000	100		4.9032		75.538		493.763		100
	13.3645	10000	10		12.0645		457.325		7355.416		10
	28.7929	100000	1		27.4929		2374.911		87044.42		1
IB	12.588	8356.321	7861254	23 units	–	1.0	–	0.9975	–	0.9982	–
	27.121	83572.23	786125		4.121		53.3595		293.1924		786125
	58.431	835747.1	78612		35.431		3944.3278		186335.3		78612
	125.886	8357516	7861		102.886		33259.732		4562614.4		7861
	271.212	83574083	786		248.212		193576.097		64063880.2		786
	584.31	835740830	79		561.31		989946.534		740889185.6		79
IC	0.8996	3.0496	400000	4 units	–	1.0	–	0.9989	–	0.9952	–
	1.939	30.5367	40000		–		–		–		
	4.1774	305.3562	4000		0.1744		0.0989		0.0234		4000
	9.0	3053.63	400		5.0		78.55		523.5988		400
	19.3899	30536.22	40		15.3899		744.1796		15268.49		40
	41.7743	305362.8	4		37.7743		4483.313		225776.06		4

[a] $U = (1 + r/r')$, $A = (1 + a/a')$, $V = (1 + v/v')$ where r', a' and $v' = \omega$, ω^2 and ω^3, respectively.

and b, in which only the data set of the model IB of Table 3 is plotted for demonstration), indicating initial power-law size distribution in the models.

Putting r and r' in place of d and d' in Eq. (3), we get:

$$N = N'(1 + r/r')^{-D} \qquad (4)$$

where N is the number of clasts of radius $\geqq r$, and N', r' and D are constants. Putting $r' = \omega$ (i.e. width of the rim that melts in each clast) in Eq. (4), the value of $(1 + r/r')$ for clast sets in the models presented in Table 3, were determined. Log–log plots of $(1 + r/r')$ vs. N give straight line graphs in each case, in contrast to the curved graphs with left-hand fall-off pattern of log N vs. log r plots (Fig. 5d and c). The R^2 value (i.e. coefficient of determination) of the regression line through the points of $(1 + r/r')$ vs. N plots in each case is 1, indicating perfect correlation (i.e. a straight line graph), whereas the regression line through the log N vs. log r plots give lower values (Fig. 5c).

Similarly, putting v and v' in place of r and r' in Eq. (4), we get:

$$N = N'(1 + v/v')^{-D} \qquad (5)$$

where N is the number of clasts of volume $\geqq v$, and N', v' and D are constants. Putting $v' = \omega^3$ in the equation, the value of $(1 + v/v')$ for clast sets in the models (Table 3), were determined. Log–log plots of $(1 + v/v')$ vs. N give straight line graphs in each case (Fig. 5f), in contrast to the curved graph with left-hand fall-off pattern of log N vs. log v plots (Fig. 5e). The R^2 value of the regression line through the points of $(1 + v/v')$ vs. N plots in each case is close to 1 ($\geqq 0.99$) indicating very good correlation. Rounding off of the figures of the numerical models at the third and fourth places of decimal at each step of calculations generated computation noise, which is why the R^2 value is close to, but not, 1 in the numerical models. Regression line through the log N vs. log v plots gives lower R^2 values (Fig. 5e).

Similarly putting $a' = \omega^2$ in the equation gives:

$$N = N'(1 + a/a')^{-D} \qquad (6)$$

where N is the number of clasts of equatorial sectional area $\geqq a$, we get regression lines for log N vs. log $(1 + a/a')$ plots, with R^2 value >0.99 (Fig. 5h). The log N vs. log a values give lower R^2 values (Fig. 5g). For further testing of these values of r', a' and v' determined by numerical modelling, several other models with all spherical clasts and initial power-law size distribution were considered. By applying uniform rim melting in stages in each model,

several sets of post-melting clast population were obtained. Each clast population was tested by putting $r' = \omega$, $a' = \omega^2$ and $v' = \omega^3$ in Eqs. (4)–(6), and similar high values of R^2 were obtained.

The preceding analysis with the help of the numerical models thus indicates that under condition of uniform rim melting, an initial (pre-melting) power-law grain size distribution pattern will not be destroyed. It will be only modified and still recognisable in the post-melting product. The modification is reflected as a 'left-hand fall-off' pattern in the log–log graphs. The modified distribution pattern follows the general relationship:

$$N = N'(1 + z/z')^{-D} \text{ or } N \propto (1 + z/z')^{-D} \qquad (7)$$

where N is number of clasts of size $\geqq z$, and N', z' and D are constants; the size z may be expressed either by volume (v) or area (a) in a section, or mean radius (r) of the clasts, and the corresponding constant will be $v' = \omega^3$, $a' = \omega^2$ or $r' = \omega$, respectively. D^v, D^a or D^r will be the modified power-law exponent, depending on which parameter is used to represent size of the clasts. The analysis further indicates that z' is related to the thickness (ω) of uniform rim melting.
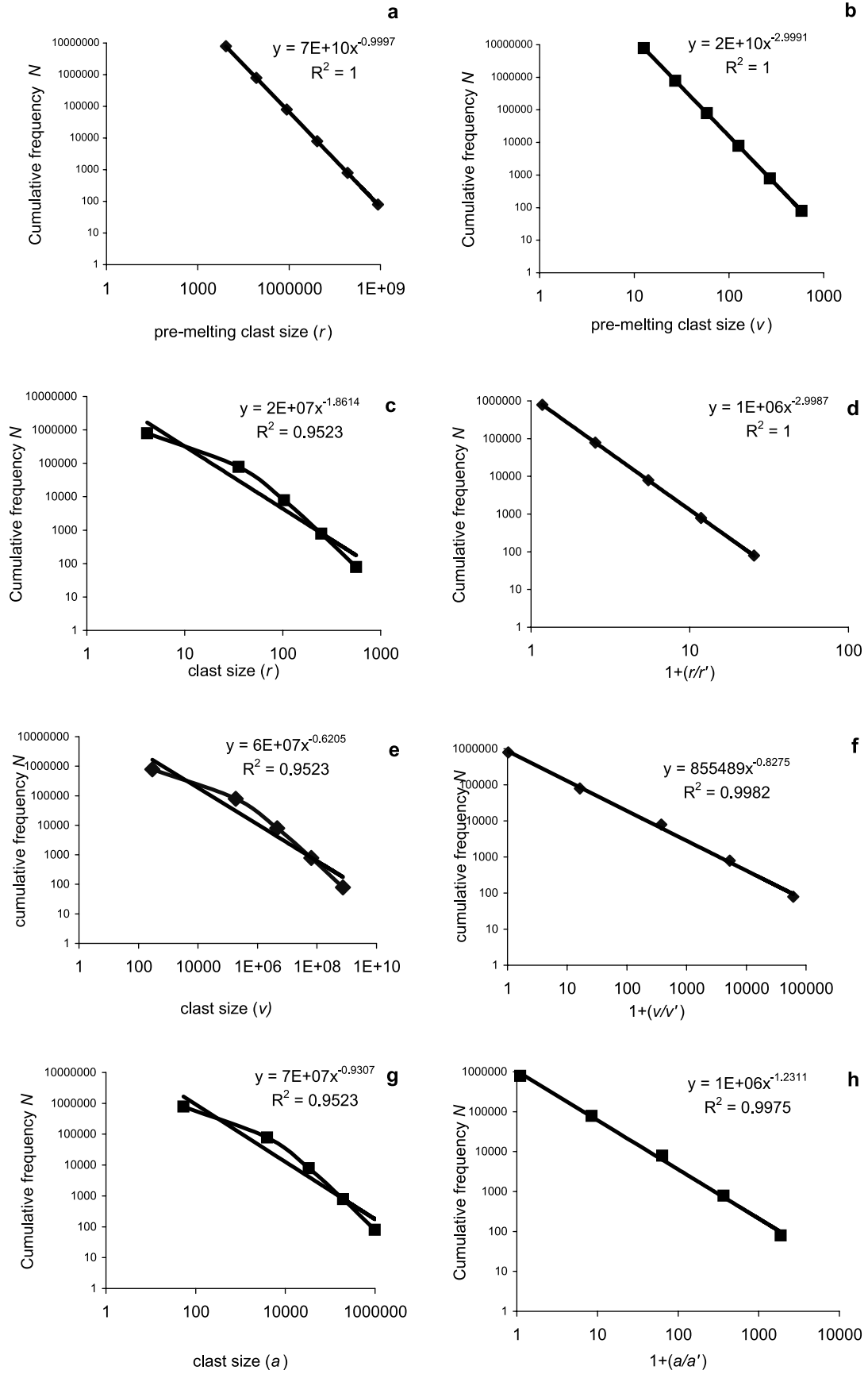
4. Microstructural features in the matrix

Backscattered electron (BSE) images of polished surfaces of the pseudotachylytes show that the rocks consist of clasts of varying sizes set in a fine-grained matrix (Fig. 6). Because of their optical contrast with the matrix, the clasts stand out prominently in BSE images. However, the nature of the matrix is variable, thus permitting recognition of the following types of matrix domains (Hetzel et al., 1996).

Microlite domains consist of a profuse development of microlites, set in an interstitial glassy material (Fig. 6a and b). *Glass domains* are those that are homogeneous and devoid of microlites (Fig. 6b).

In Fig. 6a, the microlites are concentrated in a 100–200-μm-wide zone along the contact of a pseudotachylyte vein, in which the density of microlites decreases towards the vein centre. The microlites are either needle-shaped or granular, with a few exhibiting rectangular shapes. In Fig. 6b, a narrow microlite-rich zone (about 100 μm wide) with a sharp boundary occurs within a pseudotachylyte host in which only glassy matrix is present. The dominant needle-shaped microlites are evenly distributed, whereas the granular microlites occur along the core of the zone.

Fig. 5. Log–log graphs showing effect of uniform rim melting on initial power-law clast size distribution pattern, and determination of modified power-law exponent of post-melting clast-size distribution. Only the data set of the model IB of Table 3 is considered in this diagram for demonstration. The R^2 value and equation of the regression line (the heavy line) of the point plots are given in each diagram. The exponent in each equation is slope of the regression line. (a) and (b) $R^2 = 1$ value of the regression lines of the log N vs. log r, and log N vs. log v plots of the initial (pre-melting) clast population of the model indicates power-law distribution. (c), (e) and (g) Radius (r) vs. cumulative frequency, volume (v) vs. cumulative frequency and sectional area (a) vs. cumulative frequency graphs, respectively, of post-melting clast-size distribution of the numerical model. Note that the plots define a curvilinear graph (the line joining the points), with left-hand-fall-off pattern. The regression lines have low R^2 values. (d), (f) and (h) When $(1 + r/r')$, $(1 + a/a')$ and $(1 + v/v')$ are plotted in place of radius, sectional area and volume, respectively, the plots give straight line graphs (see text). R^2 value of the regression lines is $\equiv 1$.

a $y = 7E+10x^{-0.9997}$, $R^2 = 1$ — Cumulative frequency N vs pre-melting clast size (r)

b $y = 2E+10x^{-2.9991}$, $R^2 = 1$ — Cumulative frequency N vs pre-melting clast size (v)

c $y = 2E+07x^{-1.8614}$, $R^2 = 0.9523$ — Cumulative frequency N vs clast size (r)

d $y = 1E+06x^{-2.9987}$, $R^2 = 1$ — Cumulative frequency N vs $1+(r/r')$

e $y = 6E+07x^{-0.6205}$, $R^2 = 0.9523$ — cumulative frequency N vs clast size (v)

f $y = 855489x^{-0.8275}$, $R^2 = 0.9982$ — cumulative frequency N vs $1+(v/v')$

g $y = 7E+07x^{-0.9307}$, $R^2 = 0.9523$ — Cumulative frequency N vs clast size (a)

h $y = 1E+06x^{-1.2311}$, $R^2 = 0.9975$ — Cumulative frequency N vs $1+(a/a')$

A thin mantle around some of the clasts (Fig. 6c–e) is observed in the BSE images. In some instances, only glass (Fig. 6c), or glass with rare microlites form the mantle. In Fig. 6d, granular microlites form the mantle around the clast of an alumino-silicate (?) mineral, whereas in Fig. 6e only needle-shaped microlites with interstitial glass form the mantle around a quartz clast.

4.1. Geochemistry of the microlites

Granular microlites with rectangular outline and needle-shaped microlites are the two dominant types. Chemical compositions of the needle-shaped microlites occurring along a vein contact (Fig. 6a), in the mantle zone around a mantled clast of quartz (Fig. 6e), and within a narrow pseudotachylyte vein (Fig. 6b), are given in columns 1–3, respectively, of Table 4. The compositions indicate that these needle-shaped microlites are minute crystals of ferrogedrite (Deer et al., 1983). Deer et al. (1974), reported 1.21% H_2O^+ in ferrogedrites. Addition of this proportion of H_2O in the analyses gives totals of 100.36, 98.91 and 102.59 for columns 1–3, respectively. Average chemical composition (column 4) indicates that the granular microlites occurring along the core region of the vein in Fig. 6b are minute crystals of Fe–Al spinel (hercynite; Deer et al., 1983).

4.2. Microstructural evidences of rim melting

Frictional heat generated along slip interfaces is initially transferred to the rock particles by conduction (Sibson, 1975) and leads to melting. A melt fraction is formed by accumulation and intermingling of the melt contributed by the particles of the crushed wall rock. Cataclasis and subsequent melting increase the permeability of the wall rocks of the frictional interface. The gas phase generated along with the melt (Lin, 1994; Tsutsumi, 1999) may permeate and circulate within the intergranular space of the crushed wall rocks. Initially the melt has high mobility (Sibson, 1975), and may also permeate and circulate within the crushed rocks.

The hot gas ± melt phase circulating within the inter-granular space is the heat source and each particle in the domain of melt circulation may be considered as if immersed in the hot fluid (also see fig. 11 in Ray (1999)). As already explained in the text, the heat flow will be uniform across the fluid–particle interface, and so lead to uniform rim melting of the particles.

The mobile melt, circulating in the intergranular space will assimilate and remove the films of melt formed along rim of the particles. So, evidence of rim melting at the initial stages of melt generation will not be preserved in the pseudotachylyte microstructures. The situation, however, will be different when the melt cools to a highly viscous fluid. Circulation of the melt stops because of rise in viscosity (Spray, 1993) and consequent loss of mobility.

The melt, however, will continue to supply the latent heat. The films of melt formed by rim melting of the particles at this stage will not be removed, and freeze at the site of their formation. Imprints of this late stage rim melting will be preserved, as supported by the following microstructures of pseudotachylytes from the study area.

1. The conductive–convective heat transfer (Ray, 1999) from the melt at the late stage may be adequate to completely melt the fine-grained and superfine-grained clasts that had survived up to that stage as relics. Minute droplets of melt, compositionally different from the pervading melt, were generated by this late stage melting. These droplets along with the surrounding melt congealed rapidly to produce tiny beads of glass set in a uniform groundmass of glass. Several such patches of glass have been observed (Fig. 6c), and some of the patches contain relics that have survived the process (Fig. 6f).

2. The amount of transferred heat was inadequate to completely melt the larger clasts at the late stage. Instead, only a thin film of melt, of width ω', formed along the clast rims. Chemical composition of the melt formed at the rim was subsequently modified because of mixing with the surrounding melt. Thus a melt, different in composition from the melt that initially pervaded was formed and quenched to form a mantle of glass (± microlites) around the clast (Fig. 6c–e). These mantles have sharp contacts with the glassy or microlite domains of the surrounding matrix, and are only few microns wide. Fig. 6c–e also shows that each mantle has a uniform width. So, the mantled clasts can be explained as products of late stage melting, and support the assumption of rim melting. Fig. 6f, which shows several surviving relics in a pool of glass, indicates that in highly fractured grains, melting may proceed along the fractures as well as the grain boundary.

Nucleation of microlites around the relict grains of plagioclase in pseudotachylytes was observed and explained by Maddock (1986) by 'melt-wetting' of the surfaces of the surviving feldspar grains. But such an explanation is not valid for the mantled clasts of the Sarwar–Junia sector. This is because the texture and composition of the mantles vary from clast to clast. Granular microlites form the mantle in Fig. 6d, while in Fig. 6e needle-shaped microlites with interstitial glass, and in Fig. 6c only glass form the mantles. Nucleation of microlites because of melt wetting would have produced mantles of uniform composition and texture.

5. Discussion

Assuming an initial power-law fragment size distribution pattern (Table 1a) in the numerical model, and by applying
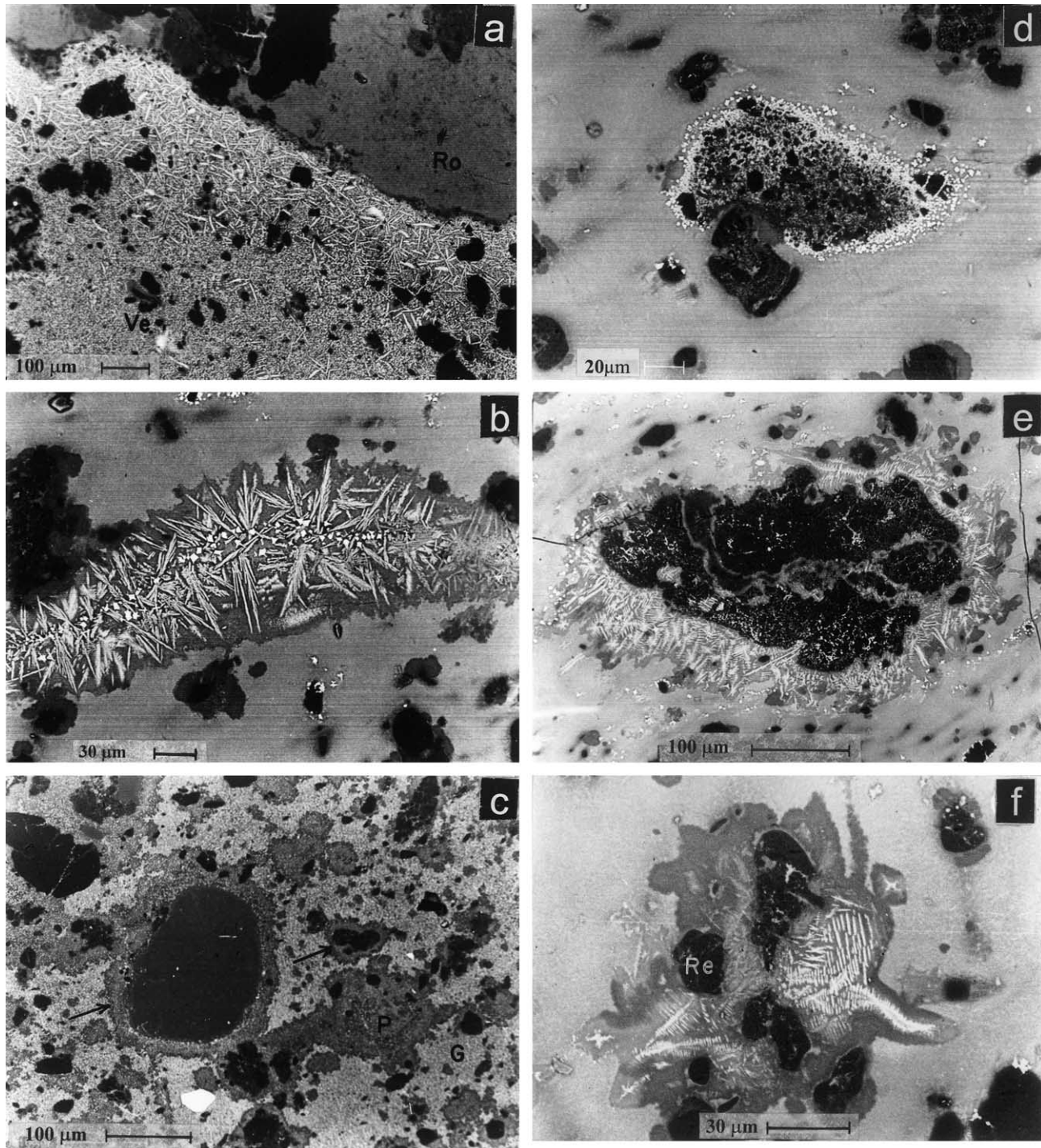
Fig. 6. Microstructures developed because of heat transfer from a melt and melt–clast interaction during pseudotachylyte generation (backscattered electron images, all photographs taken on LEO S440 SEM). (a) Profuse development of microlites along the contact of a pseudotachylyte vein (Ve) with the intact country rock (Ro). (b) Granular and the needle-shaped microlites with interstitial glass in a narrow zone within a pseudotachylyte vein. (c) Mantles of glass (at the arrowheads) formed because of rim melting of clasts. Patches of glass (P) within a groundmass of glass (G) of different chemical composition have formed because of late-stage melting (see text) of small-size clasts. (d) Mantle of granular microlites (hercynite) around a clast. (e) Mantle of needle-shaped (ferrogedrite) microlites with interstitial glass around a quartz clast. (f) Late-stage melting of a clast has formed a tiny bead of glass containing relicts (Re). The tiny patch is engulfed by a structureless glassy matrix of lighter grey colour.

uniform rim melting of the fragments, we obtained a post-melting clast-size distribution pattern that is in close agreement with the size–frequency distribution pattern observed in the clast population of natural pseudotachylyte

samples from the Sarwar–Junia sector in western India (Ray, 1999). A consistent 'left-hand fall-off' pattern, comparable with that predicted by the numerical models, was recorded in natural (Ray, 1999, figs. 4 and 12) and

Table 4
Chemical composition of the microlites in different microstructural domains

	1	2	3	4
SiO_2	41.93 ± 2.09	48.80 ± 2.48	45.13 ± 1.69	0.45 ± 0.38
Al_2O_3	14.31 ± 2.83	15.83 ± 0.69	17.70 ± 1.32	52.81 ± 3.92
Na_2O	0.11 ± 0.09	0.64 ± 0.56	0.295 ± 0.007	–
K_2O	0.615 ± 0.13	2.96 ± 0.83	1.98 ± 0.40	0.13 ± 0.01
MgO	11.66 ± 1.09	7.04 ± 1.23	9.67 ± 0.14	3.65 ± 1.07
FeO	28.69 ± 0.54	19.93 ± 3.25	24.58 ± 2.37	38.81 ± 3.32
CaO	0.31 ± 0.04	0.98 ± 1.26	0.27 ± 0.10	0.03 ± 0.04
MnO	0.46 ± 0.09	0.25 ± 0.13	0.22 ± 0.007	0.20 ± 0.13
BaO	0.005 ± 0.01	0.05 ± 0.04	–	0.05 ± 0.02
Cr_2O_3	0.035 ± 0.02	0.02 ± 0.03	0.07 ± 0.08	1.25 ± 1.12
TiO_2	0.97 ± 0.09	1.12 ± 0.08	1.555 ± 0.23	0.32 ± 0.26
P_2O_5	0.018 ± 0.03	0.05 ± 0.06	0.06 ± 0.08	0.005 ± 0.007
NiO	0.03 ± 0.04	0.002 ± 0.004	0.05 ± 0.06	0.12 ± 0.17
CoO	0.005 ± 0.01	0.026 ± 0.03	–	0.05 ± 0.06
Number of probe analysis	4	5	2	2

(1)–(3) The needle-shaped microlites (ferrogedrite) occurring (1) along a vein contact, (2) in the mantle zone of a mantled clast, and (3) within the microlite zone of a narrow pseudotachylyte vein. (4) Granular microlites (hercynite) within a narrow vein. Average and standard deviation are given for the multiple analyses. Each analysis is of a separate microlite or glass occurrence. A CAMECA SX51 Electron Probe Microanalyser was used for the laboratory analyses. The operating conditions were: 15 kV high voltage, 12 nA current, with a 1 micron diameter beam. Natural mineral standards were used.

experimentally generated (Tsutsumi, 1999, fig. 2a–d) pseudotachylytes. Moreover, Ray (1999, fig. 4) observed that the power-law exponent in a coarser size fraction is higher than that in the finer size fraction. This is in agreement with the findings of the numerical model.

The close agreement between the results of the numerical models and the clast-size analyses of natural and experimentally generated pseudotachylyte samples validates the assumptions of (1) an initial power-law fragment size distribution pattern, and (2) uniform rim melting applied in the models. Moreover, validity of both the assumptions can be independently established. The results of studies on simulated fault gouges (already discussed) supports initial power-law clast-size distribution generated by pre-melting crushing of wall rocks. The microstructural features and numerical models support uniform rim melting of the clasts.

Recent research has revealed that the matrix in many pseudotachylytes is a mixture of finely crushed material and quenched melt (Magloughlin, 1992; Shimamoto and Nagahama, 1992; Spray, 1995; Hetzel et al., 1996; Ray, 1999; Tsutsumi, 1999), thereby indicating pseudotachylyte generation by a combination of cataclasis and melting of fault rocks, in which cataclasis precedes melt generation. The present study indicates that cataclasis generates the power-law fragment-size distribution pattern, which is subsequently modified because of uniform rim melting. So, we may conclude that a modified power-law distribution pattern is a characteristic feature of clasts in all varieties of fault-related pseudotachylytes, including the clast-poor varieties, which occur as fault veins and injection veins.

Some workers have suggested that the number of fine clasts, smaller than about 5 μm size, would be very small because of complete dissolution of fine clasts in a hot melt (Shimamoto and Nagahama, 1992). Such a conclusion,

however, is not tenable because, if heat supply is adequate to melt grains of diameter $2\omega'$, the grains of size $(2\omega' + \delta)$ will survive as clasts of size δ, where δ may have any value from fraction-of-a-micron upwards. So superfine clasts will also be present, and there is no possibility of abrupt reduction of their proportion after post-seismic melting. The reduction of proportion of fine clasts would be gradual, as is reflected by the gentle left-hand fall-off pattern of the log–log graphs of size–frequency distribution in clast-laden pseudotachylytes (Ray, 1999, figs. 4 and 12).

6. Conclusions

1. Frictional heat generated at fault interfaces leads to melting of a rim of approximately uniform thickness in each grain of the crushed wall rocks. By this process, the initial power-law size distribution pattern of the crushed rocks is only modified and not destroyed by subsequent melting. Size distribution of the relicts, which occur as clasts in pseudotachylytes, shows this modified pattern.

2. This modification is reflected in the log–log graphs of cumulative frequency against size of the clasts, as a 'left-hand fall-off' pattern.

3. The modified distribution pattern obeys the general equations $N = N'(1 + z/z')^{-D}$, or $N \propto (1 + z/z')^{-D}$, where N is number of clasts of size $\geqq z$, and N', z' and D are constants. The size z may be expressed either by mean radius (r), sectional area (a) in a section or volume (v) of the clasts. D is the modified power-law exponent of clast-size distribution.

4. This modified power-law distribution pattern is characteristic of clast population of all varieties of fault-generated pseudotachylytes, irrespective of the genetic process involved.

5. The constant z' (i.e. r', a' or v', depending on whether radius, sectional area or volume of the clasts is measured) depends on thickness (ω) of uniform rim melting. The values obtained are $r' = \omega$, $a' = \omega^2$, and $v' = \omega^3$.
6. Minute droplets of glass within the glassy matrix and the mantled clasts bear evidence of the rim melting process.

Acknowledgements

References

Balasundaram, M.S., 1969. Geological and mineral map of Rajasthan. (1:2.25 million scale). Geological Survey of India, Calcutta.

Deer, W.A., Howie, R.A., Zussman, J., 1974. Rock-Forming Minerals. Volume 2, Longman, UK.

Deer, W.A., Howie, R.A., Zussman, J., 1983. An Introduction to the Rock-Forming Minerals, The English Language Book Society and Longman, England.

Geological Survey of India, 1977. Geology and mineral resources of the states of India. Part XII. Rajasthan. Miscellaneous Publication, No. 30, Geological Survey of India, Calcutta.

Heron, A.M., 1953. The geology of central Rajputana. Memoir Geological Survey of India 79(1), 1–389.

Hetzel, R., Altenberger, U., Strecker, M.R., 1996. Structural and chemical evolution of pseudotachylytes during seismic events. Mineralogy and Petrology 58, 33–50.

Lin, A., 1994. Glassy pseudotachylyte veins from the Fuyun fault zone, northwest China. Journal of Structural Geology 16, 71–83.

Maddock, R.H., 1983. Melt origin of fault-generated pseudotachylytes demonstrated by texture. Geology 11, 105–108.

Maddock, R.H., 1986. Partial melting of lithic porphyroclasts in fault-generated pseudotachylytes. Neues Jahrbuch Fur Mineralogie Abhandlungen 155, 1–4.

Magloughlin, J.F., 1992. Microstructural and chemical changes associated with cataclasis and frictional melting at shallow crustal levels: the cataclasite–pseudotachylyte connection. Tectonophysics 204, 243–260.

Magloughlin, J.F., Spray, J.G., 1992. Frictional melting processes and products in geological materials: introduction and discussion. Tectonophysics 204, 197–204.

Marone, C., Scholz, C.H., 1989. Particle-size distribution and microstructures with simulated fault-gouge. Journal of Structural Geology 11(7), 799–814.

McKenzie, D., Brune, J.N., 1972. Melting on fault planes during large earthquakes. Royal Astronomical Society Geophysical Journal 29, 65–78.

Philpotts, A.R., 1964. Origin of pseudotachylytes. American Journal of Science 262, 1008–1035.

Ray, S.K., 1999. Transformation of cataclastically deformed rocks to pseudotachylyte by pervasion of frictional melt: inferences from clast-size analysis. Tectonophysics 301, 283–304.

Sammis, C.G., King, G., Biegel, R., 1987. The kinematics of gouge deformation. Pure and Applied Geophysics 125, 777–812.

Shand, S.J., 1916. The pseudotachylyte of Parijs (Orange Free State). Geological Society of London Quarterly Journal 72, 198–221.

Shimamoto, T., Nagahama, H., 1992. An argument against a crush origin for pseudotachylytes based on the analysis of clast-size distribution. Journal of Structural Geology 14, 999–1006.

Sibson, R.H., 1975. Generation of pseudotachylyte by ancient seismic faulting. Royal Astronomical Society Geophysical Journal 43, 775–794.

Spray, J.G., 1987. Artificial generation of pseudotachylyte using friction welding apparatus: simulation of melting on a fault plane. Journal of Structural Geology 9(1), 49–60.

Spray, J.G., 1993. Viscosity determinations of some frictionally generated silicate melts: implications for fault zone rheology at high strain rates. Journal of Geophysical Research 98(B5), 8053–8068.

Spray, J.G., 1995. Pseudotachylyte controversy: fact or friction? Geology 23(12), 1119–1122.

Tsutsumi, A., 1999. Size distribution of clasts in experimentally produced pseudotachylytes. Journal of Structural Geology 21, 305–312.

Turcotte, D.L., 1997. Fractals and Chaos in Geology and Geophysics, Cambridge University Press, UK.